Plasma Physics and
Controlled Fusion

PAPER • **OPEN ACCESS**

Long pulse H-mode operation in JET-ITER like wall

To cite this article: E Lerche *et al* 2025 *Plasma Phys. Control. Fusion* **67** 095022

OPEN ACCESS
IOP Publishing
Plasma Physics and Controlled Fusion
Plasma Phys. Control. Fusion **67** (2025) 095022 (18pp)
https://doi.org/10.1088/1361-6587/ae006f

Long pulse H-mode operation in JET-ITER like wall

E Lerche[1,2,*], D King[2], X Litaudon[3], S Brezinsek[4], E Joffrin[3], R Lobel[2], F Auriemma[5], M Beldishevski[2], N Balshaw[2], M Baruzzo[5,6], A Boboc[2], P Card[2], I S Carvalho[7], P Carvalho[2], I Coffey[2], P McCullen[2], S Dalley[2], E Delabie[2,8], P Dumortier[1], R Felton[2], N Fonnesu[6], S Gerasimov[2], Z Ghani[2], A Goodyear[2], N Hawkes[2], R Henriques[2], S Hotchin[2], P Jacquet[2], I Jepu[2], D Keeling[2], D Kinna[2], K Kirov[2], D Kos[2], E Litherland-Smith[2], P Lomas[2], C Lowry[2], J Mailloux[2], M Maslov[2], D Matveev[4], A Meigs[2], S Menmuir[2], J Mitchell[2], I Monakhov[2], C Noble[2], M Poradzinski[2,9], F Rimini[2], S Silburn[2], E R Solano[10], H Sun[2], C Srinivasan[2], B Thomas[2], D Valcarcel[2], D Van Eester[1], R Villari[6], J Waterhouse[2], A West[2], I Young[2], JET Contributors[11], the EUROfusion Tokamak Exploitation Team[12] and the JET Operations Team[13]

[1] Laboratory for Plasma Physics, ERM/KMS, TEC partner, Brussels, Belgium
[2] UKAEA, CCFE, Culham Campus, Abingdon, United Kingdom
[3] CEA, IRFM, St-Paul-Lez-Durance, France
[4] Forschungszentrum Juelich, IEK-4, Juelich, Germany
[5] Consorzio RFX (CNR, ENEA, INFN), Padova, Italy
[6] ENEA, Fusion and Nuclear Safety Department, C.R. Frascati, Rome, Italy
[7] ITER Organization, Route de Vinon-sur-Verdon, CS 90 046 13067, St. Paul Lez Durance Cedex, France
[8] Oak Ridge National Laboratory, Oak Ridge, TN, United States of America
[9] Institute of Plasma Physics and Laser Microfusion, Warsaw, Poland
[10] Laboratorio Nacional de Fusión, CIEMAT, Madrid, Spain

E-mail: Ernesto.Lerche@ukaea.uk

Received 29 April 2025, revised 21 August 2025
Accepted for publication 28 August 2025
Published 12 September 2025

Abstract

In the last experimental campaign of the JET tokamak in December 2023, long duration discharges in deuterium plasmas were performed to assess the sustainment of the plasma performance over many resistive time scales and to address plasma-wall interaction physics in a full metallic environment with the ITER-like wall (ILW), featuring a W divertor and a Be first wall (Matthews *et al* 2011 *Phys. Scr.* **2011** 014001; Neu *et al* 2011 *Plasma Phys. Control. Fusion* **53** 124040). Two types of long duration discharges were developed: (i) a 30 s flat-top ELMy H-mode with combined 12–14 MW neutral beam injection (NBI) and 2 MW of ion-cyclotron resonance heating (ICRH) and (ii) a 60 s long pulse with 4–6 MW of NBI during

[11] See Maggi *et al* 2024 (https://doi.org/10.1088/1741-4326/ad3e16) for JET Contributors.
[12] See Joffrin *et al* 2024 (https://doi.org/10.1088/1741-4326/ad2be4) for the EUROfusion Tokamak Exploitation Team.
[13] See King *et al* 2024 (https://doi.org/10.1088/1741-4326/ad6ce5) for the JET Operations Team.
[*] Author to whom any correspondence should be addressed.

the entire flat-top and 2 MW of ICRH for about 40 s. The pulses were stationary from the radiation point of view without sign of core impurity accumulation and featured regular type-I ELMs with roughly equilibrated ion and electron temperatures in most cases. The discharges required significant technical adjustments in many subsystems, ranging from plasma shape control, machine protection and diagnostic settings (King *et al* Technical and Engineering challenges for long pulses on JET ITER). The experiments achieved the maximum energy ever injected in a single pulse in JET ($E_{\mathrm{IN}} = 450$ MJ) and challenged the operational domain of the inertially cooled divertor limits. An overview of the main properties of these discharges in terms of plasma stationarity, ELM behavior, plasma-wall interaction and overall performance will be presented and the contribution of these unprecedented JET-ILW results to the multi-machine CICLOP (Coordination on International Challenges on Long duration Operation) database (Litaudon *et al* 2024 *Nucl. Fusion* **64** 015001) will be highlighted.

Keywords: JET-ILW, long pulse operations, CICLOP

1. Introduction

JET was the largest tokamak in operation from 1983 until 2023. From 2011 onwards it was equipped with a full metallic wall referred to as the ITER-like wall (ILW) [1, 2], consisting of a tungsten (W) divertor and beryllium (Be) plasma facing components. It has been decided to maintain the acronym JET-ILW, despite the fact that all plasma facing surfaces in ITER are now expected to be W from first plasma. The first years of the JET-ILW operation focused on developing high performance deuterium scenarios in a full metallic environment [3–12] and on studying the plasma-wall interaction and fuel retention physics [13–20] in high power conditions in view of ITER's and future fusion reactor's operation. More recently, dedicated Deuterium–Tritium (D–T) fusion experiments were performed [21–23] and different high-performance scenarios were tested [24–30], culminating in the world-record fusion energy ever achieved in a tokamak [31, 32] and a clear demonstration of α-particle effects by different techniques [33–36].

Despite its outstanding contribution to fusion physics in various domains, JET is not a super-conducting device nor has actively cooled plasma facing components since it was not originally designed for long plasma discharges and steady-state fusion studies. Nevertheless, before the end of JET's operation in December 2023, it was decided to stretch the machine capabilities to their limits and assess the potential of doing long pulses ($t \approx 60$ s) with good plasma performance. The last time such long pulses were attempted was in the early 90 s with a Carbon wall, using combined lower hybrid current drive (LHCD) and ion cyclotron resonance heating (ICRH) resulting in dominant electron heating [37]. Since then, JET has undergone a large number of upgrades—aside from the change in the wall material—and the focus was mainly on the performance of the heating systems [38–41], enhanced diagnostics in view of D–T operation [42–44] and machine protection schemes for disruption mitigation and wall protection in view of ITER [45–47]. In the most recent machine configuration, LHCD was mothballed and is not available for operation but the neutral beam injectors (NBI) were upgraded to sustain full power (1.5–2.0 MW) with each of the 15 actively cooled positive ion source injectors (PINIs) available for a time window of 15 s [38]. The ICRH system can provide 18 s continuous heating power per antenna pair, with a total of 2 antenna pairs (B and D) connected in ELM-resilient configurations [41] with $P \approx 2$ MW each. If the requested magnetic field is kept below $B_0 < 2.4$ T, static power units alone can provide enough current to the toroidal field coils to sustain it for a few minutes and the B_0 flat-top duration is only restricted by the ohmic heating limits ($\mathrm{I^2T}$) of the actively cooled copper coils and their differential expansion with respect to the structural components that do not carry current [48]. In these conditions, the main constrains for long pulse operation are the available poloidal flux (to inductively drive the plasma current) and the inertially cooled divertor energy limits. By combining the independent heating power units in an optimized time-sequence in view of sustaining high electron temperature during the heating phase (therefore maintaining the plasma resistivity low enough for minimizing the flux consumption) and by adapting the plasma shape dynamically to spread the heat loads on the inertially cooled divertor tiles, long duration discharges with high performance up to 60 s were deemed achievable for the first time in JET-ILW, addressing engineering and physics issues.

Two types of long duration deuterium discharges were envisaged: (i) 30 s high power H-mode pulses with two successive windows of 12–14 MW NBI heating combined with 2 MW of ICRH and (ii) 60 s long pulses with four 15 s windows of 4–5 MW NBI and 2 MW ICRH for 36 s. Throughout the paper, 'pulse duration' refers to the high-performance flat-top phase of the discharge, i.e. the phase with constant plasma current, constant magnetic field and maximum auxiliary power available. A schematic of the heating waveforms proposed for the two types of long pulses is shown in figure 1. The magnetic field was chosen to be $B_0 = 1.9$ T at the magnetic axis for allowing central hydrogen minority ICRF heating at a frequency of 29 MHz (the lowest frequency available with reliable power coupling capabilities) while a plasma current of $I_{\mathrm{P}} = 1.4$ MA was chosen for its moderate requests in terms of flux consumption based on the plasma resistivity

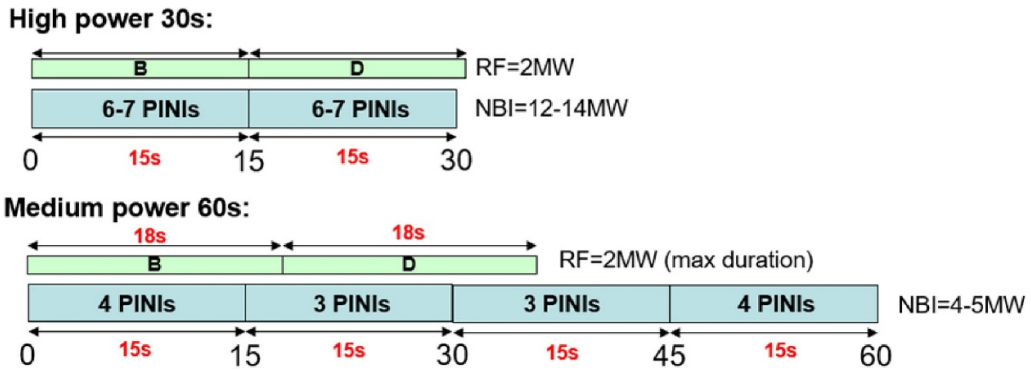

Figure 1. Schematics of the NBI and ICRH power waveforms used for the high power 30 s and the medium power 60 s discharges with 14 NBI injectors (PINIs) and 2 sets of ICRF antenna arrays (B, D).

expected with the heating power available. In addition, plasmas with similar parameters had already been developed in JET-ILW but with shorter duration [6, 49, 50] and showed robust plasma start-up, good performance and low MHD activity, which relieved the risk of developing a dedicated scenario from scratch for the long pulses and allowed to build on past experience for the initial phase of the discharge.

To comply with the (inertially cooled) divertor energy handling capabilities in JET-ILW, the convected power on the divertor had to be shared between different divertor plates for long pulse/high injected energy operation. For this, the location of the strike points was shifted during the discharges from the horizontal divertor plate Tile 6 or 'corner configuration' (characterized by stronger pumping with the outer strike point close to the pumping throat) to the vertical divertor plate Tile 7 (with lower pumping capability). The position of the strike points with respect to the JET-ILW divertor geometry is illustrated in figure 2 from the EFIT reconstructions of the magnetic equilibria for the 2 cases. The global shape parameters calculated by EFIT are similar for both configurations (minor radius = 0.9/0.9 m, elongation at separatrix = 1.68/1.69, triangularity = 0.34/0.31, for Tile 6/Tile 7 respectively) but the Tile 7 configuration is slightly shifted upwards and is less triangular so that the minimum wall clearance between the plasma and the outer limiter is located above the mid-plane and is somewhat reduced w.r.t. the Tile 6 configuration, min. gap = 4.5 cm (Tile 7) instead of 6 cm (Tile 6). Despite the small variations in the global magnetic configuration, the change in the strike point location has very strong consequences on the plasma performance and particularly on the ELM behavior, as will be discussed later.

Aside from the topics discussed above, the development of the long pulses described here required significant technical and tokamak operation adjustments in many subsystems, ranging from plasma shape control, machine protection and diagnostic systems settings, all managed by the central JET control and data acquisition system [51]. A comprehensive review of the engineering and operational steps that made such pulses possible in JET are given by *D. King et al* in this same

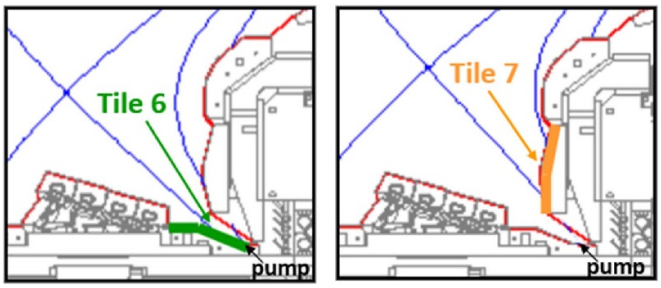

Figure 2. Magnetic equilibrium calculated with EFIT (#105468) illustrating the strike point positions of the two magnetic configurations used for the long pulses in JET-ILW: Horizontal target or 'corner' configuration (Tile 6) and vertical target (Tile 7).

journal issue [48]. Another topic for which these experiments made an important contribution was in the context of the water activation measurements being developed for ITER and future fusion reactors [52]. These experiments profited from the long-lasting neutron exposure during the long pulses to measure and model the characteristic time delays between the actual D–T neutron generation and the neutronic diagnostics in the NBI cooling water loop set-up [53].

The paper is organized as follows: In sections 2 and 3, the high power 30 s and the medium power 60 s discharges will be described, with focus on plasma performance, discharge stationarity, ELM-behavior and plasma-wall interaction aspects. The latter is described in more detail in [54]. In section 4, the key results of the interpretative TRANSP simulations performed for the 30 s and 60 s long pulses are described and analyzed. Section 5 presents the contribution of the JET-ILW long pulse results to the international database from the 'Coordination on International Challenges on Long duration Operation (CICLOP)' group [55], with particular focus on the relatively high confinement time and central ion temperatures obtained in JET as compared to other devices with long pulse operation capability. The paper ends with a brief summary and a discussion of potential physics challenges encountered during the development of the long pulse discharges in JET.

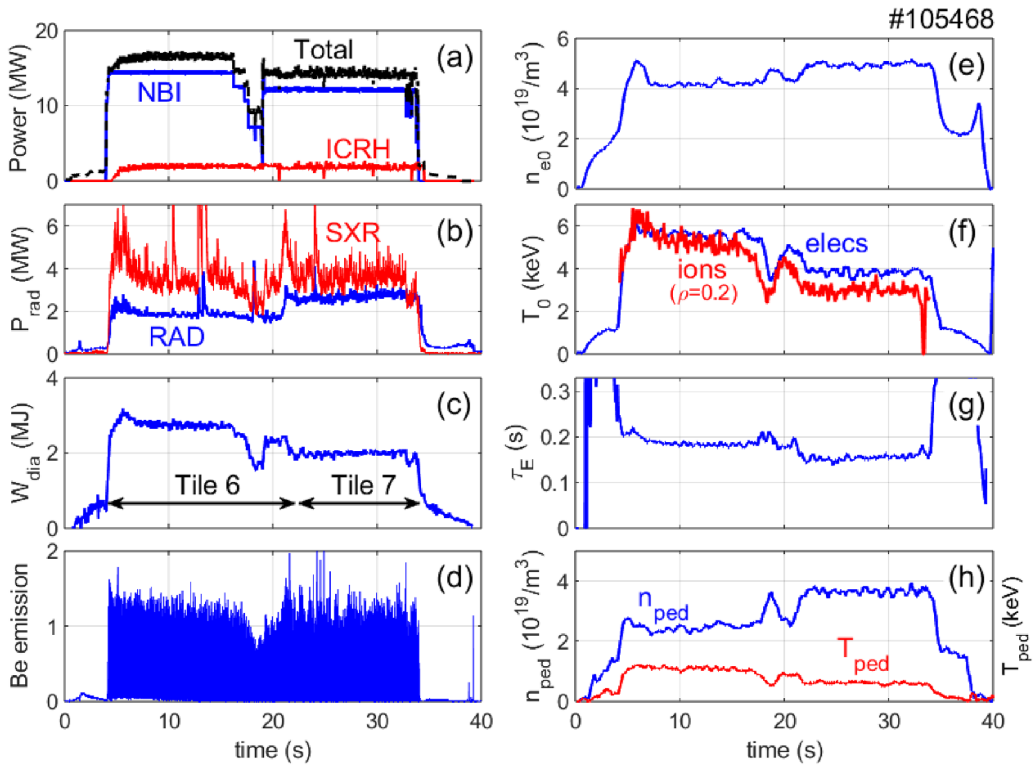

Figure 3. Time traces of the best high power 30 s discharges achieved (#105468): (a) NBI and ICRH powers; (c) bulk radiated power (bolometer) and central soft x-ray emission (SXR); (c) plasma stored energy; (d) be-I emission (visible spectroscopy); (e) central electron density (HRTS); (f) core electron (HRTS) and ion (CXRS/XCS) temperatures; (g) energy confinement time (EFIT); (h) pedestal density and temperature (HRTS).

2. High power 30 s discharges

For the plasma discharges aiming at 30 s flat-top, approximately 13–15 MW NBI and 2 MW ICRF power were available. For the selected magnetic field ($B_0 = 1.9$ T) and plasma current ($I_P = 1.4$ MA), this power level leads to a moderate density ($n_{e0} = 4$–5×10^{19} m^3) H-mode discharge with type-I ELMs throughout, as illustrated in figure 3. This pulse features the largest total injected energy ever achieved in JET, $E_{IN} = 450$ MJ, and challenged the operational domain of the inertially cooled divertor limits, reaching a total energy convected to the divertor plates of $E_{DIV} = 365$ MJ, shared between Tile 6 and Tile 7. As mentioned earlier, the strike point is shifted from Tile 6 (stronger pumping) to Tile 7 (weaker pumping) at $t = 21.5$ s for keeping acceptable energy input levels on each of the divertor plates. The input energy limits allowed for Tile 6 and Tile 7 for standard operation are $E_{IN} = 315$ MJ and $E_{IN} = 444$ MJ, respectively, and assume a minimum radiated power fraction of 20% and a power sharing relation of 2:1 between the outer and the inner divertor plates [48]. These energy limits were imposed to reduce the fatigue on the divertor structures to ensure successful completion of the D–T experimental campaigns, and do not represent the energy values for which actual damage is expected in the divertor plates. The strike point position has strong consequences on the plasma performance. After the shape transition from Tile 6 to Tile 7, the plasma stored energy (c) is reduced from $W_{dia} = 2.8$ MJ ($\beta_N = 2.3$) to $W_{dia} = 2$ MJ ($\beta_N = 1.6$) and the bulk radiated power (b) measured by bolometry [56, 57], which is modest overall, increases from $P_{rad} = 2$ MW to 3 MW. These values are in line with the decrease of the energy confinement time (g) form $\tau_E = 0.2$ s to $\tau_E = 0.15$ s when moving the strike-point to Tile 7. The Z_{eff} values inferred from visible spectroscopy at the plasma edge [58] were similar, $Z_{eff} = 1.8$ (Tile 6) and $Z_{eff} = 1.9$ (Tile 7), being dominated by emission from light impurities such as Beryllium and Neon. The central electron temperature (f)—from High-Resolution Thomson scattering (HRTS) [59]—decreases from $T_{e0} = 5.5$ keV to about 4 keV while the central plasma density (e) increases from $n_{e0} = 4 \times 10^{19}$ m^3 to 5×10^{19} m^3 when moving the strike point from Tile 6 to Tile 7, because of the less efficient pumping in the latter conditions. The core ion temperature $T_{i,\rho=0.2}$ follows closely the central electron temperature evolution but is slightly lower throughout the discharge (f). This is mainly because the ion temperature signal shown in figure 3(f) is not measured at the magnetic axis but at about 20 cm off-axis ($\rho \approx 0.2$), as a combination of charge-exchange recombination spectroscopy (CXRS) [60, 61] and x-ray crystal spectroscopy (XCS) [62] measurements. Hence, it represents an underestimated value for the actual T_{i0} evolution in the discharge, which could be up to 20% higher when the NBI deposition is central (see figure 4(f) for a comparison between the T_e and T_i profiles). The impact on the pedestal density and temperature time evolution are even more evident (h), as will be discussed later. The lower plasma performance in the Tile 7 configuration was already documented in other experiments

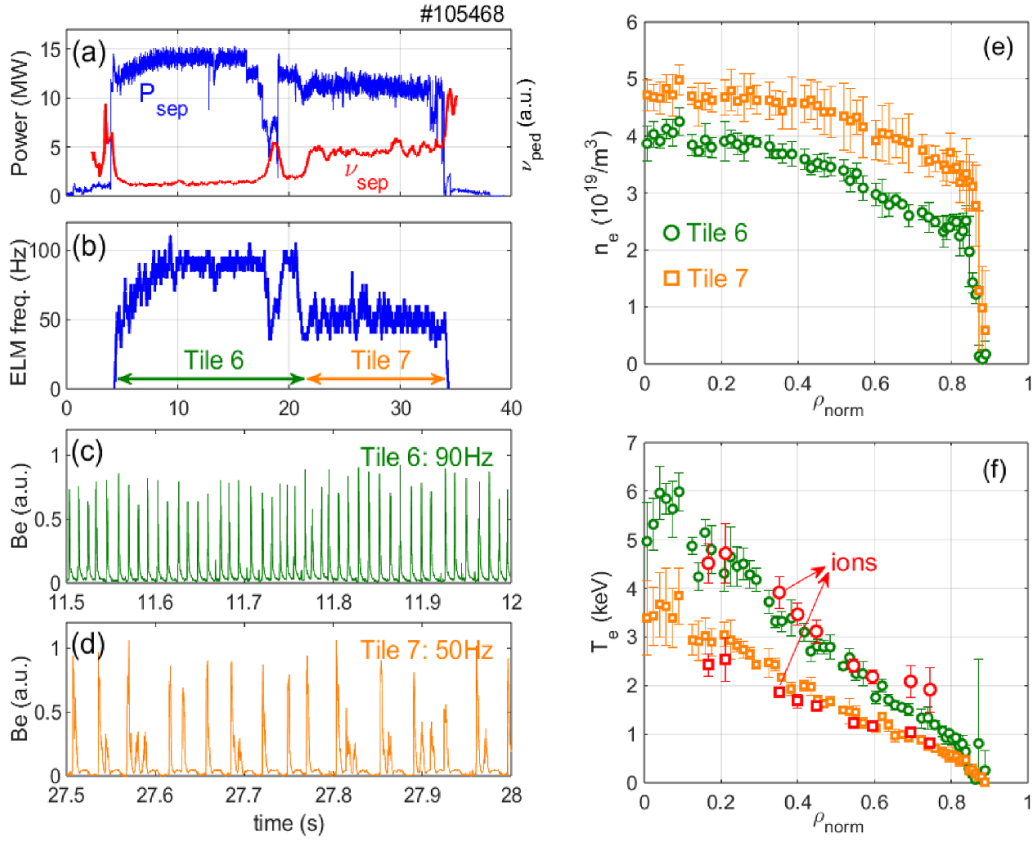

Figure 4. ELM behaviour in pulse #104568 when the strike-point is located on Tile 6 or on Tile 7: (a) power through the separatrix $P_{sep} = P_{IN} - P_{rad,\,bulk}$ and pedestal collisionality (a.u.); (b) ELM frequency; (c, d) be-I emission. Kinetic profiles measured during the Tile 6 (circles) and Tile 7 (squares) phases: (e) electron density profiles (HRTS); (f) electron temperature profiles (HRTS) and ion temperature profiles (core CXRS) as function of the normalized toroidal flux coordinate.

in JET [63, 64] and in this particular discharge is exacerbated by the lower NBI power available in the second part of the discharge, but the effect of the strike point position is still dominant. The central ion temperature suffers from a stronger decrease than the electron temperature because the NBI power is lower and its deposition is more off-axis, most of the central deposition injectors having been used in the first part of the pulse in order to obtain the beam related diagnostic data. Attempts to optimize the second half of the discharge (e.g. by reducing the gas injection or increasing the NBI power) proved only marginally efficient, confirming the strong shape dependence of the discharge performance. Despite the decrease in performance and increase in total radiation in the second half of the pulse, the discharge remains stationary from the impurity accumulation point of view, as seen by the constant radiation time trace and from the central soft x-ray (SXR) emission signal shown in figure 3(b). The spikes observed in the signals are small impurity influxes which only have a transient effect on the radiation signals and do not impact the global plasma performance, confirming that these plasmas are robust in terms of avoiding impurity accumulation. A detailed edge impurity transport study as reported in [65] could not be done at these high ELM frequencies due to limitations in the temporal resolution of the diagnostic signals needed but the conditions suggest that ELM-flushing of the high-Z impurities is the dominant effect in these discharges, the ion temperature gradients outside the pedestal not being large enough for neoclassical impurity screening to be efficient [25, 66]. Pulse #105468 only used ca. 70% of the available ohmic flux, as a combination of the relatively low plasma resistivity (low Z_{eff}, large T_e) and a non-negligible fraction of bootstrap current (see section 4).

Although pulse #105468 is stationary from the radiation point of view and stays in type-I ELMy regime throughout the flat-top, the ELM behavior is quite different in the two phases of the discharge, as shown in figure 4: during the Tile 6 phase, the ELM frequency is about 90 Hz while it is reduced to approximately 50 Hz during the Tile 7 phase. This is a consequence of the higher pedestal density and lower pedestal temperature (larger pedestal collisionality) reached in the Tile 7 phase, as shown in figures 4(e) and (f). This evolution changes the stability of the ELMs in the peeling-ballooning diagram [67] and strengthens resistive effects in the ELM dynamics [68]. The lower input power (and higher radiation) during the Tile 7 phase exacerbates this effect in this particular pulse, but the main change in the ELM dynamics comes from the larger pedestal collisionality and resistivity, which are substantially increased during the Tile 7 phase (see

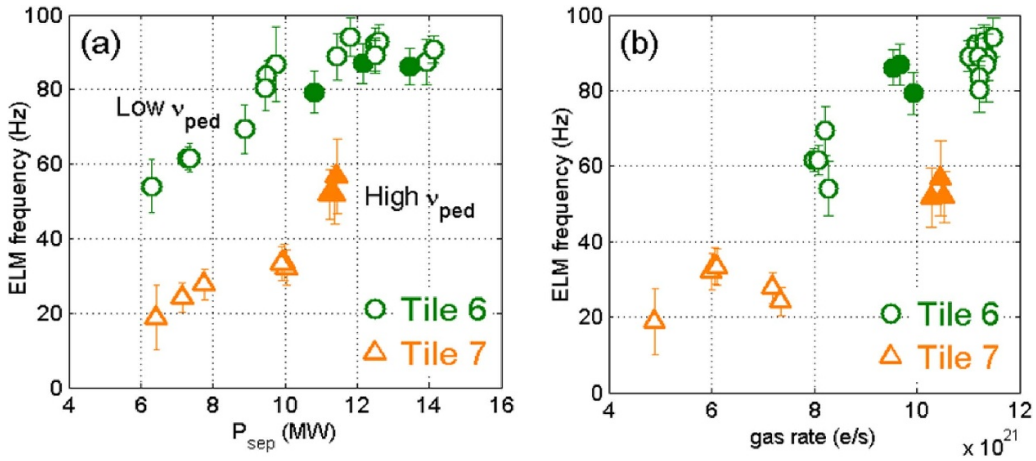

Figure 5. (a) ELM frequency as function of P_{sep} for Tile 6 and Tile 7 strike point operation; (b) ELM frequency as function of the injected (D_2) gas rate. The solid symbols compare pulse #105468 on Tile 6 with pulse #105474 on Tile 7, with similar P_{sep} and gas rate values showing lower natural ELM frequency on Tile 7.

figure 4(a)). Note that the SOL diagnostics were not available in this discharge and the HRTS data is unreliable outside the separatrix and hence has been omitted in figures 4(e) and (f).

The power flowing through the separatrix is defined as $P_{sep} = P_{IN} - P_{rad,bulk}$, where P_{IN} is the total input power (ohmic + NBI + ICRH) and $P_{rad,bulk}$ is the power radiated inside the separatrix measured by bolometry [56, 57]. To disentangle the effect of the power through the separatrix P_{sep} from the pedestal conditions on the ELM dynamics for the two strike point configurations used, a power scan was performed in a series of discharges similar to #105468. The results are shown in figure 5(a): while the ELM frequency increases with the value of P_{sep} in both cases, it is systematically higher when the strike-point is on Tile 6. To match the Tile 7 ELM frequency to the one observed on Tile 6, a significantly larger P_{sep} would be needed. The gas injection rate also impacts the ELM frequency in these discharges (figure 5(b)) but its value is systematically lower on Tile 7 in the gas range studied (5–12 $\times$ 10^{21} e s^{-1}). The full symbols represent two discharges with similar gas injection and P_{sep} values and confirm the lower ELM frequency when the strike point is located on Tile 7 (vertical target, lower pumping) for otherwise similar engineering parameters. This is very interesting data for ELM stability analysis [69] but a detailed study is left outside of this paper.

Another topic considered in these experiments was the heat exhaust on the divertor in a non-actively cooled environment. Because the radiation levels are low in these pulses ($P_{rad}/P_{IN} < 20\%$), the divertor captures most of the power lost through the separatrix. Figure 6(c) shows the divertor temperature measured by an infra-red (IR) camera with a top view [15] in a 27 s long pulse with slightly less averaged input power (#105585, $P_{IN} = 15$ MW) than the record energy shot (#105468, $P_{IN} = 17$ MW) shown in figure 3. Unlike the latter, this pulse was performed with the strike point deliberately kept on Tile 6 only and required special authorization to run since the input energy estimated before the pulse exceeded the operation limit imposed on Tile 6 for standard plasma operation, $E_{IN} = 315$ MJ.

The divertor surface temperature rises strongly after the NBI power is switched-on and saturates around 900 °C towards the end of the discharge ($t > 20$ s), where the NBI power is reduced to 11 MW and the ICRF power is between 2–4 MW. The divertor reaches thermal equilibrium due to the conductive heat exchange with the neighbouring structures and black-body radiation losses, which are not negligible at these temperatures for Tungsten. The final temperature reached is well below the trip protection level (1200 °C in this discharge) but the total energy input ($E_{IN} = 365$ MJ) exceeded the maximum value set for standard operation on Tile 6, as shown in figure 6(b). The energy deposited in the divertor after subtracting the radiation losses reaches $E_{DIV} = 305$ MJ at the end of the pulse and is consistent with the 20% radiated power fraction assumption used in the energy limit checks done before the pulse execution. Thermocouple measurements processed after the discharge confirm that the actual energy deposited on Tile 6 in pulse #105585 exceeded, for the first time in JET-ILW, the energy limit imposed on Tile 6 for the so called 'orange-band' operation [48]. When the NBI is reduced at 27 s, the temperature falls rapidly and reaches a new equilibrium value of approximately 850 °C. After the pulse the divertor surface temperature decrease is much slower because the whole tile structure became warmer and, in some cases, a long inter-pulse wait time is needed, depending on the energy input expected for the next shot. The spikes observed in the temperature signal represent the ELM heat-load footprint on the divertor.

3. Medium power 60 s long discharges

For the 60 s duration plasmas, 4 $\times$ 15 s windows of NBI with 5–6 MW and 2 $\times$ 18 s windows of ICRH with 2 MW were used. The heating strategy was adapted by the fact that ICRH

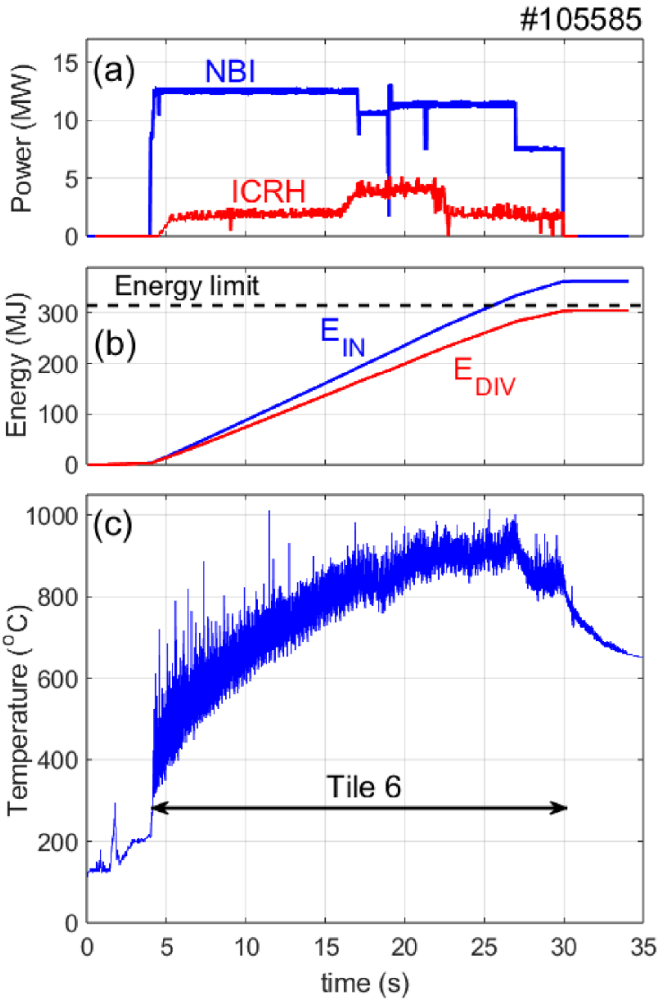

Figure 6. (a) NBI and ICRH input power, (b) total input energy E_{IN} and energy reaching the divertor ($E_{\mathrm{DIV}} = E_{\mathrm{IN}}$-$E_{\mathrm{rad}}$); (c) surface temperature of the divertor Tile 6 measured with an infra-red camera (top view). The dashed line in panel (b) indicates the input energy limit for standard operation with the strike point on Tile 6 (315 MJ).

would not be able to cover the full pulse length so more NBI power was left available for the second part of the discharge to compensate the ICRH reduction. The divertor power handling recipe was also different from the 30 s discharges: the pulse starts with a 10 s phase with the strike point located on Tile 7 and then transits to Tile 6 for the rest of the discharge. This approach was developed to increase the plasma performance as long as possible and to enhance the plasma stationarity (e.g. avoid potential impurity accumulation), since the ELM frequency is expected to be larger on the Tile 6 configuration and only marginal on Tile 7 for the amount of input power available. Several of these pulses challenged the energy limit allowed on the Tile 6 divertor plate without any detectable consequences.

An example of the 60 s flat-top discharge achieved in JET (#105750) is given in figure 7. Between 4–6 MW of NBI was applied throughout the flat-top and 2 MW ICRH were coupled during the first 36 s (a). The averaged stored energy (c) is constant around $W_{\mathrm{dia}} = 1.6$ MJ with central electron temperatures (measured by ECE radiometry [70]) of $T_{\mathrm{e0}} = 3.5$ keV and ion temperatures at $\rho = 0.2$ of $T_{\mathrm{i0}} \approx 3.0$ keV (f) during the combined NBI + ICRH heating phase. The reduction of the ion temperature observed at $t = 22$ s is believed to be exaggerated by the change in NBI injector combination which influenced the central CXRS measurements. The electron and ion temperatures drop after the ICRF switch-off but the energy remains approximately constant, as a combination of the slightly higher plasma density and lower radiation. The energy confinement (g) is also roughly constant $\tau_E = 0.25$–0.3 s, slightly higher than the values obtained in the high-power 30 s pulses described in section 2. This is due to the power degradation effects observed in JET at medium input power levels [71], pretty much in line with the IPB98(y,2) energy confinement scaling [72]. The radiation level is pretty low (in particular during the Tile 6 phase of the discharge) and there is no sign of impurity accumulation despite the large W event seen at $t = 34$ s, as also illustrated by the central SXR emission measurements shown in the same panel as the radiation (b). During the initial Tile 7 phase ($t < 15$ s), the radiation is higher and the central SXR signal is increasing, suggesting marginal core impurity control in these conditions. This is due to the unfavorable ELM behavior during this phase, as will be discussed later. The Z_{eff} value estimated from edge spectroscopy is $Z_{\mathrm{eff}} = 1.65$ throughout, including during the NBI-only phase of the discharge. The pedestal density is, as expected, higher between ELMs during the Tile 7 phase of the pulse (h) while the pedestal temperature does not increase after the transition from Tile 7 to Tile 6. This is different from what was observed in the high power 30 s pulses (where T_{ped} was clearly higher on Tile 6 at constant input power) and is believed to be related to the lower separatrix power seen in the 60 s pulses. Discharge #105750 consumed about 80% of the available ohmic flux, and could be extended by ca. 15 s if the NBI power could be extended and up to 25 s if both NBI and ICRH would remain available until the end of the discharge, as discussed in [48]. Finally, note that the HRTS measurements (figures 7(e) and (h)) were interrupted at $t = 60$ s, but from other signals such as the plasma energy (c) or the ECE electron temperature (f) one can see that pulse #105750 was terminated successfully without a disruption.

The ELM behaviour is also different from the one observed in the high power 30 s pulses, as illustrated in figure 8. During the short Tile 7 phase, the ELMs are completely irregular (d) because the input power is too marginal to keep the discharge in H-mode regime. During the Tile 6 phase, with only slightly higher power through the separatrix due to lower radiation, $P_{\mathrm{sep}} = 6$ MW, type-I ELMs are clearly visible (c). The ELM frequency is comparable to the one observed in the 30 sec pulses (ca. 60 Hz) but their amplitude is smaller as visible from the Be emission signal (same scale as in figure 3). The ELM frequency is very sensitive to the input power (or rather P_{sep}), suggesting that this pulse is very close to the L–H power threshold in general, estimated around 4.5 MW in

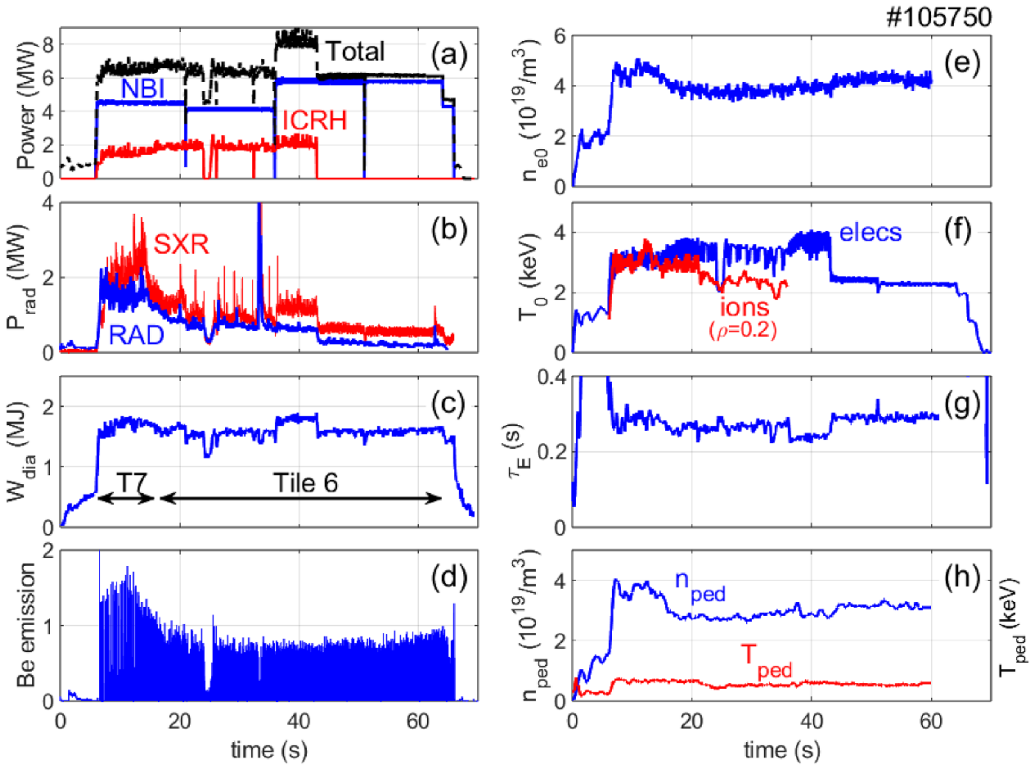

Figure 7. Time traces of the 60 s discharge achieved (#105750): (a) NBI and ICRH powers; (c) radiated power (bolometer) and central soft x-ray emission (SXR); (c) plasma stored energy; (d) be-I emission signal; (e) central electron density (HRTS); (f) core electron (ECE) and ion (CXRS/XCS) temperatures; (g) energy confinement time; (h) pedestal density and temperature (HRTS). The ion temperature measurements are only available until $t = 35$ s and the HRTS acquisition was stopped at $t = 60$ s.

this discharge (see figure 8(a)). The L–H power threshold signal shown in figure 8(a) is estimated from *Martin's* scaling law described in [73], which does not take credit for the strike point location. More recent studies unveiled a more complex L–H power threshold behavior as function of both the strike point location [64] and the plasma density [11, 27], but the estimates given in [73] are appropriate for the density range of the pulses described here ($n_{e0} \approx 5 \times 10^{19}$ m^{-3}, $f_{GW} \approx 0.7$) and for the discussion that follows.

Despite of the moderate input power ($P_{IN} \approx 6$ MW) discharge #105750 reaches H-mode with type-I ELMs, with a frequency ranging from 50–90 Hz during the Tile 6 phase, depending on the power through the separatrix, P_{sep}. The sensitivity of the ELM regime to P_{sep} is depicted in figure 9: for $P_{sep} = 6$ MW, type-I ELMs with ca. 60 Hz are observed. When the power drops by 2 MW at 24 s (figure 9 (left)), the ELMs disappear in about 150 ms ($\approx \tau_E/2$) and the plasma enters a marginal H-mode regime with coherent edge $N = 0$ MHD oscillations called 'M-mode' [74] at JET ('I-phase' in AUG), confirming the proximity to the L–H transition threshold (see figure 8(a)). When the power is increased by 2 MW (figure 9—right), the ELM frequency increases from 60 to 90 Hz. Note that the transient power drop between 35.9 s and 36 s shown in figure 9 (right) is too short with respect to the energy confinement time to have a noticeable impact on the ELM dynamics.

The sensitivity of the ELM frequency as function of the power through the separatrix P_{sep} is further illustrated in figure 10: Above the approximate value of the L–H power threshold of $P_{sep} = 4.5$ MW, the ELM frequency increases rapidly with power, changing by 45 Hz with a variation of $\Delta P_{sep} = 2$ MW, as shown before. Around $P_{sep} = 5$ MW, only a few ELMs are large enough to be detected by the ELM frequency calculation procedure and the apparent ELM frequency is lower (≈30 Hz) than in reality. Below this value the plasma enters the 'M-mode' regime and the edge oscillations are too small to be detected by the ELM counter. The gas injection rate was kept constant in this dataset, $\Gamma = (8.0 \pm 0.4) \times 10^{21}$ elec s^{-1}.

The final analysis of this section illustrates the heat loads in the divertor tiles during the 60 s long discharge #105750. Figure 11(c) shows the time evolution of the surface temperature measured by an IR camera (top view) on Tile 6 as a response to the input power applied, shown in figure 11(a). The temperature signal during the initial Tile 7 operation phase ($t < 16$ s) has to be taken cautiously, since the IR camera has a top view and the strike point is on a very tangential line of sight, so the measurement does not reflect the actual Tile 6 surface temperature but rather a mixture between reflection of the heat loads induced on Tile 7 and the actual heat loads reaching Tile 6. After the transition to Tile 6 the divertor reaches thermal equilibrium around 550 °C with $P_{IN} = 6$ MW but starts to

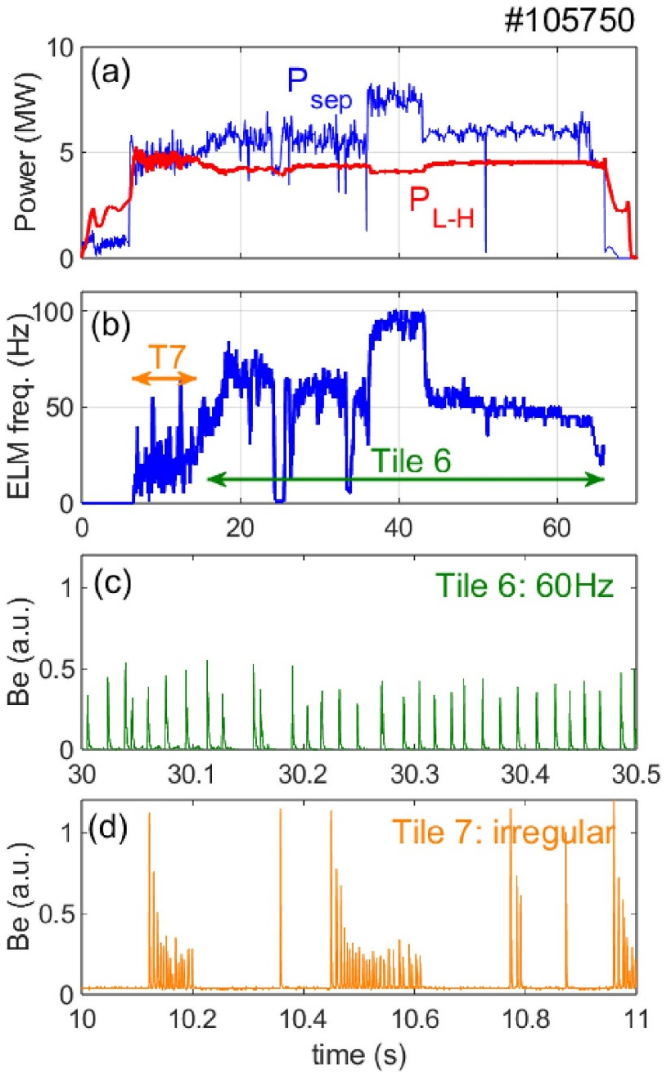

Figure 8. ELM behavior in pulse #105750 when the strike-point is located on Tile 6 or on Tile 7: (a) power through the separatrix $P_{sep} = P_{IN} - P_{rad,bulk}$ and predicted L–H power threshold; (b) ELM frequency; (c), (d) be-I emission on Tile 6 and Tile 7 (same scale as in figure 4).

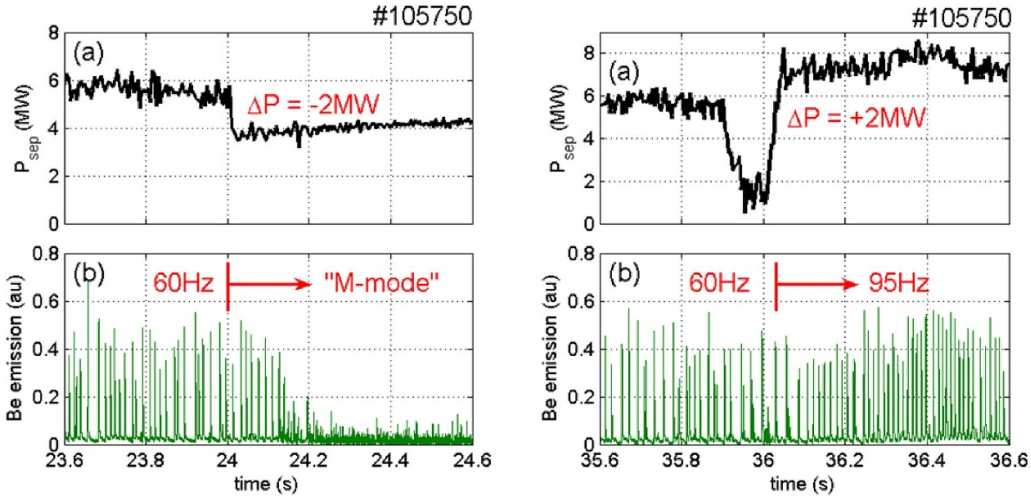

Figure 9. Effect of a power drop (left) and power increase (right) on the ELM frequency in discharge #105750: (a) Power through the separatrix ($P_{sep} = P_{IN} - P_{rad,bulk}$); (b) be-I emission signal.

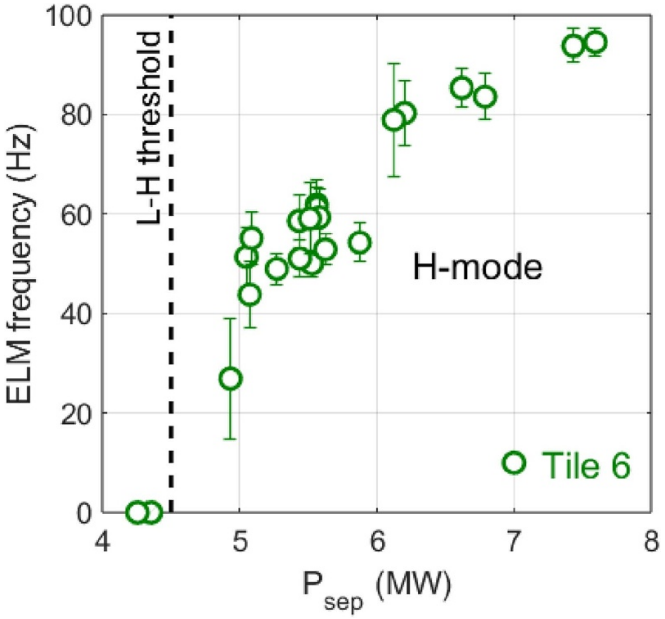

Figure 10. ELM frequency as function of the power flowing through the separatrix ($P_{sep} = P_{IN} - P_{rad,bulk}$) for operation on the Tile 6 divertor plate. The L–H power threshold is approximately 4.5 MW in all the pulses used.

increase when 2 MW of NBI power is added at $t = 37$ s. It increases by ca. 200 °C in less than 10 s and tends to saturate around 750 °C–800 °C, but before it reaches saturation the ICRF power is switched-off. After this, the temperature drops by approximately 50 °C and features a slow and gradual increase with $P_{IN} = P_{NBI} = 6$ MW until the end of the discharge. Unlike for the 30 s pulses and despite of the lower input power, the divertor temperature never reaches thermal equilibrium in this pulse due to the lower conductive power exchange capabilities and lower black body radiation losses at lower divertor plate temperatures. The maximum temperatures measured in the inner-wall and outer-wall Be limiters were practically constant from $t = 20$ s and never exceeded 400 °C, which is well below the safety limit for the Be wall protection (850 °C). No localized hot-spots were detected either.

Discharge #105750 was again one of the few pulses that ever exceeded the Tile 6 divertor energy limit in JET-ILW, as shown in figure 11(b), with a special authorization to run in these conditions. Note that the input energy during the Tile 6 operation phase was relatively close to the energy limit value of 315 MJ ($E_{IN} = 322$ MJ) but because of the very low radiation losses during the Tile 6 phase (see figure 7(b)), the actual energy reaching the divertor plates was larger than originally expected with 20% of prescribed radiation losses, reaching $E_{DIV} = 296$ MJ at the end of the pulse.

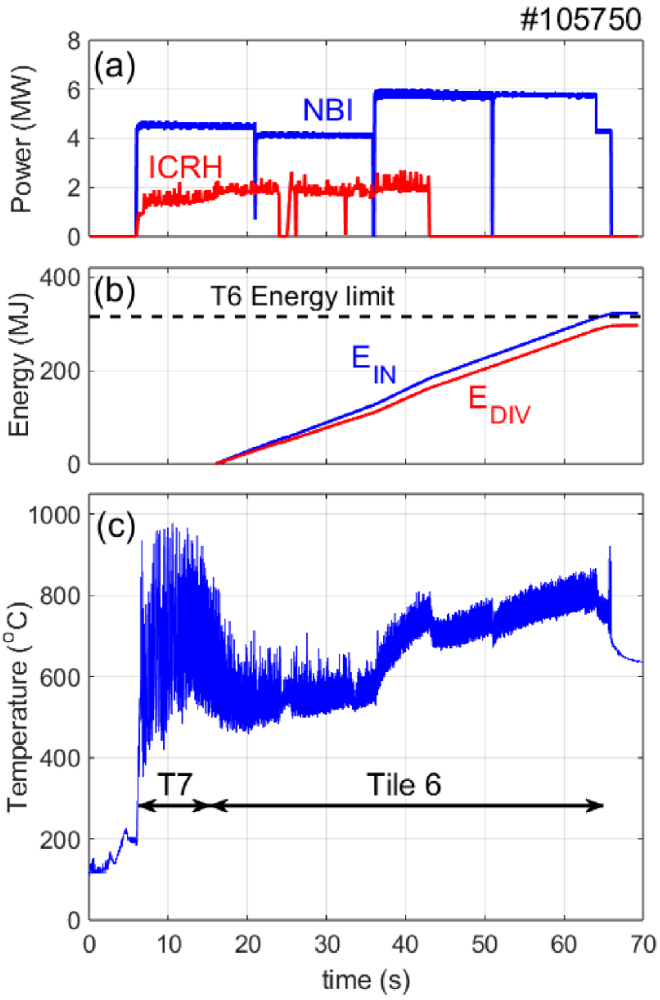

Figure 11. (a) NBI and ICRH input power, (b) total input energy E_{IN} during the Tile 6 phase and energy reaching the divertor ($E_{DIV} = E_{IN} - E_{rad}$); (c) surface temperature of the divertor Tile 6 measured with an infra-red camera. The dashed line in panel (b) shows the Tile 6 energy limit for standard operation (315 MJ).

4. TRANSP simulations

Interpretative TRANSP simulations [75], using as input the measured kinetic plasma profiles, were performed for many of the long discharges reported in this paper. Aside from allowing to estimate some physics quantities of interest that are not directly measured (such as the electron and ion heating profiles, fast particle parameters, the current diffusion time, etc…), one of the main objectives of these simulations was to check the consistency between the different quantities measured experimentally, in particular to assess whether the core ion temperature measurements—which were difficult to estimate in these pulses due to the lack of central neutral beam power during the full duration of the pulses—were reliable. The inputs used in the simulations were produced using pressure constrained EFIT equilibrium data [76] and the reference kinetic profiles were reconstructed from a combination of various diagnostics using OMFIT [77]. See [78] and references therein for a detailed description of the procedures used for preparing and running the TRANSP (V24.0.1) simulations at JET.

Figures 12 and 13 show some of the TRANSP results obtained for the 30 s long pulse #105468. The input power is shown in figure 12(a) and the corresponding central electron densities and temperatures are similar to the values shown in

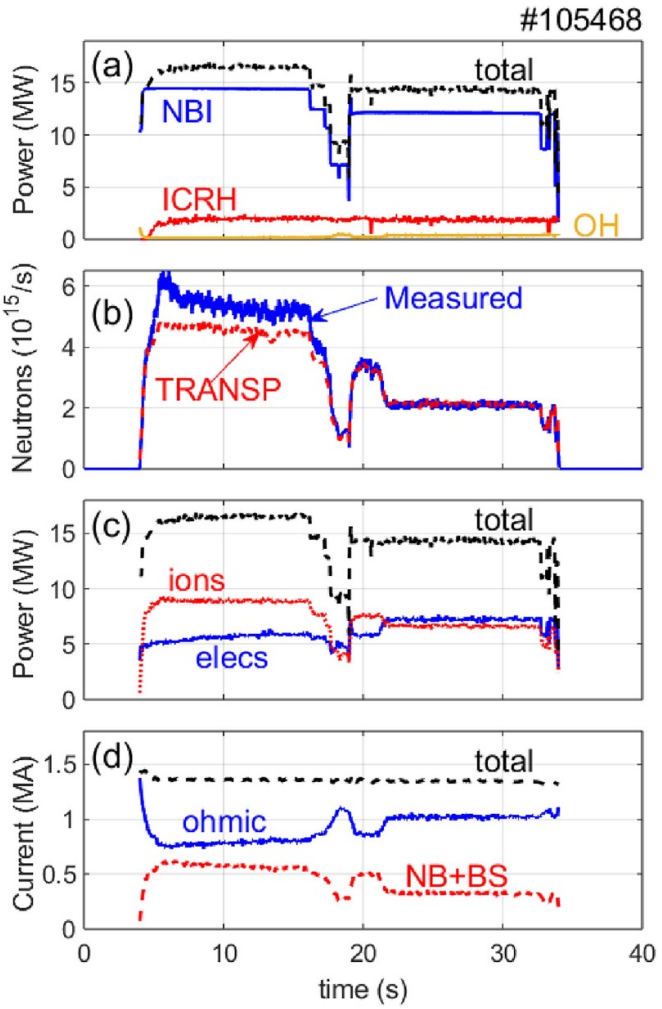

Figure 12. TRANSP results for pulse #105468 assuming $T_i = T_e$: (a) input power; (b) neutron rate; (c) electron and ion heating; (d) ohmic and non-inductive currents.

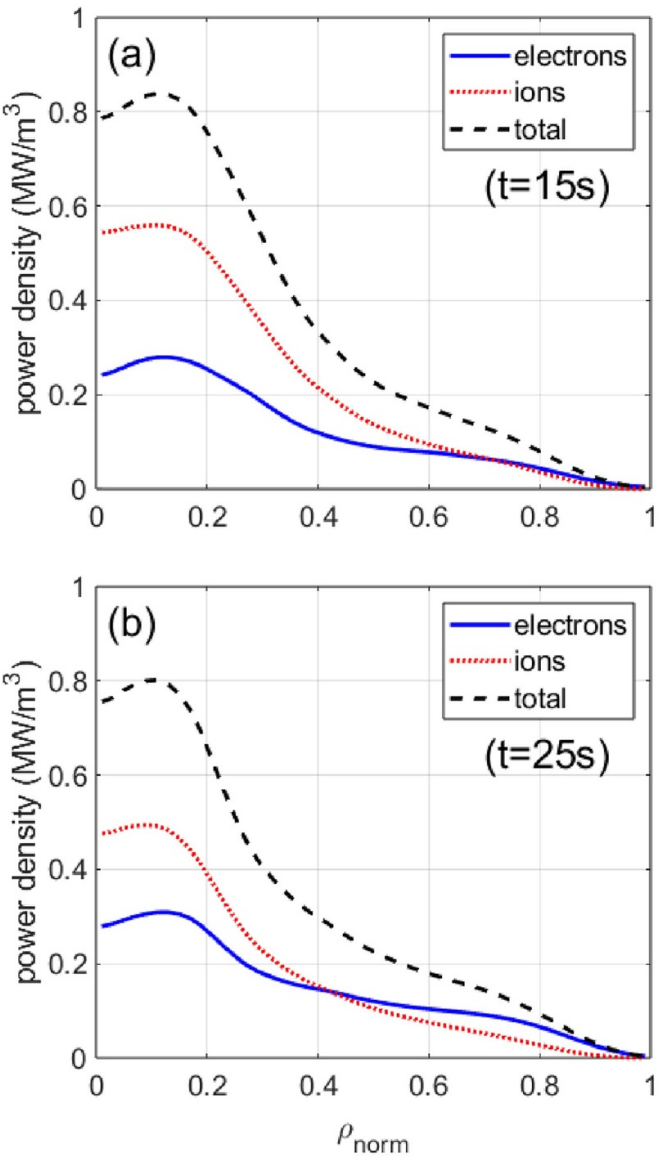

Figure 13. Total power deposition profiles to electrons and ions computed by TRANSP for pulse #105468 at $t = 15$ s (a) and $t = 25$ s (b).

figures 3(e) and (f), respectively. Examples of the n_e and T_e profiles are also given in figure 4. For these simulations, the ion temperature profiles were assumed to be the same as the electron temperature ones ($T_i = T_e$) during the entire discharge duration.

Figure 12(b) shows the comparison between the calculated and the measured neutron rates. In the first part of the discharge (Tile 6), the neutron rate is underestimated by TRANSP, suggesting that the core ion temperature is higher than the electron one, which is consistent with figure 3(f) that shows T_i ($\rho = 0.2$) $\approx T_e$ ($\rho = 0$) in this phase. In the second part of the discharge, the neutron rates are perfectly matched indicating that $T_i = T_e$ is a good approximation. This is not consistent with the time traces shown in figure 3(f) which indicate $T_i < T_e$ in the plasma core during this phase of the discharge. Figure 12(c) shows the total (NBI + ICRH + ohmic) power being absorbed by the electrons and by the ions. The results confirm dominant ion heating in the first part of the discharge and balanced electron-ion heating in the second part, supporting the temperature discussions above. The radial power deposition profiles to ions and electrons are shown in figure 13 at $t = 15$ s (a) and $t = 25$ s (b). It is interesting to note that even if the integrated values show equilibrated ion and electron heating in the second phase of the pulse (figure 12(b)), the central power deposition to ions remain dominant, the total (integrated) electron power having a strong contribution from the off-axis NBI deposition. Finally, figure 12(d) shows the fraction of ohmic and non-inductive current drive by NBI and bootstrap current (NB + BS) to the total plasma current of $I_P = 1.4$ MA. The non-inductive current fraction reaches 40% during the initial Tile 6 phase and decreases to 25% during the Tile 7 phase of the discharge because the plasma density increases—leading to a reduction of the bootstrap and neutral beam currents—and because of the lower electron temperature which leads to a higher plasma resistivity. This is also confirmed by the loop voltage measurement (not shown) which changes from 120 mV during the Tile 6 phase to 220 mV after

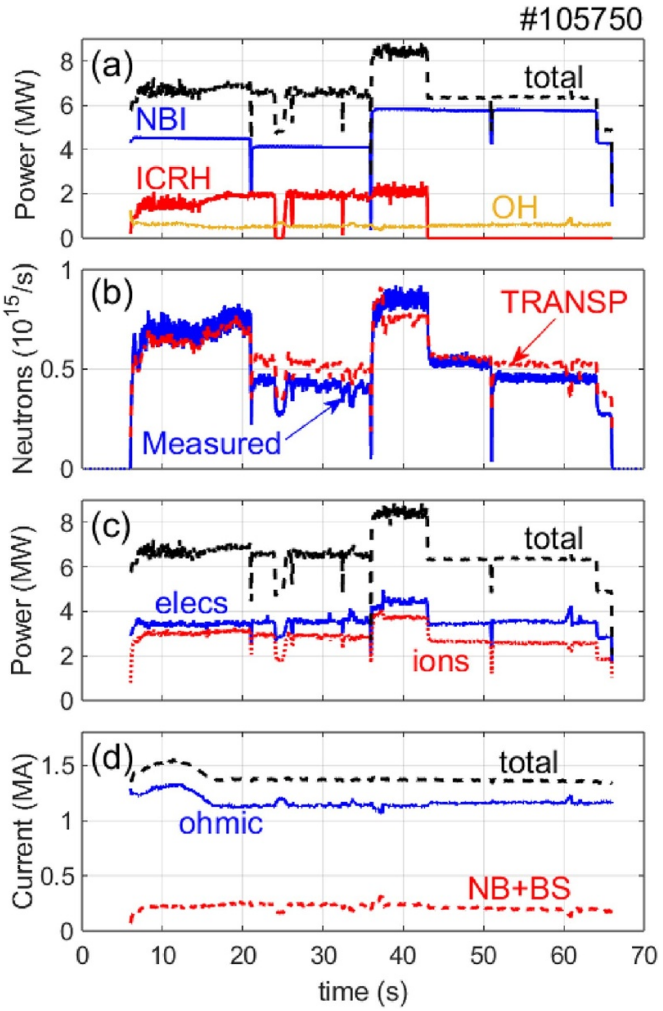

Figure 14. TRANSP results for pulse #105750 assuming $T_i = T_e$: (a) input power; (b) electron and ion heating; (c) neutron rate; (d) ohmic and non-inductive currents.

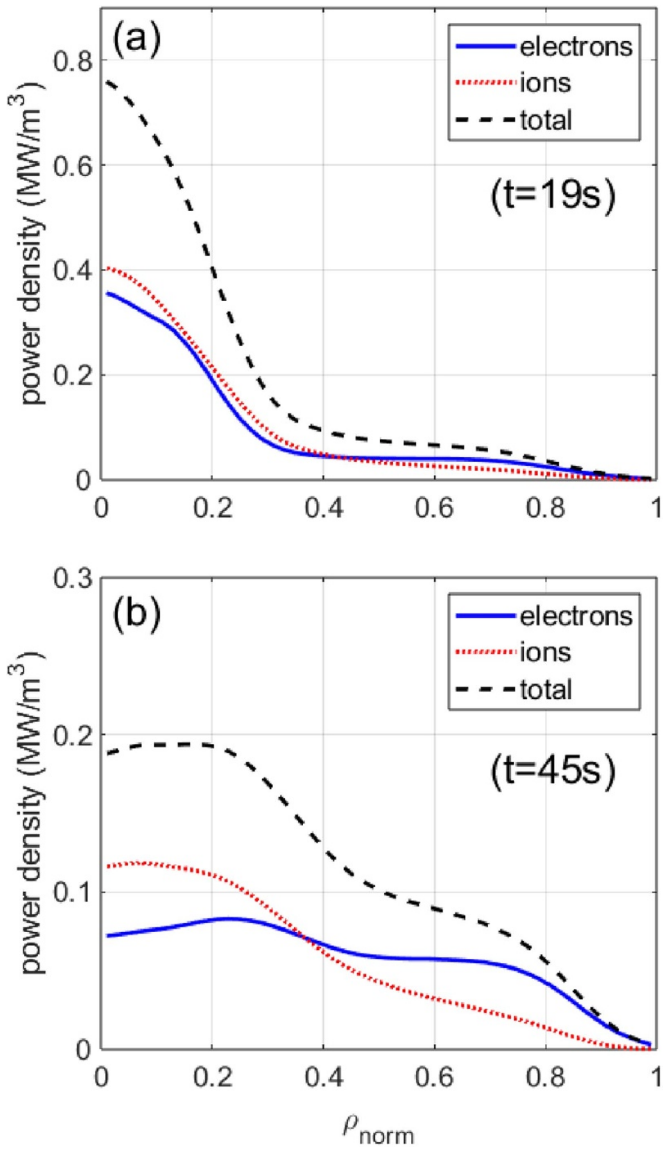

Figure 15. Total power deposition profiles to electrons and ions computed by TRANSP for pulse #105750 at $t = 19$ s (a) and $t = 45$ s (b).

the transition to Tile 7. It is worth mentioning that the bootstrap current of $I_{BS} = 350$ kA reached in the first part of pulse #105468 is one of the highest ever achieved in JET. The current diffusion time based on the neo-classical resistivity [79] computed by TRANSP at $\rho_{norm} = 0.5$ is about $\tau_d \approx 35$ s during the Tile 6 operation phase and $\tau_d \approx 20$ s during the Tile 7 phase (lower T_e). This suggests that pulse #105468 was not yet long enough for the current profile to reach steady state in these conditions.

Figures 14 and 15 show the TRANSP results obtained for the 60 s long pulse #105750. Again, the input power is shown in figure 14(a) and the corresponding central electron densities and temperatures used as input for the simulations are consistent with the ones shown in figures 7(e) and (f), respectively. The ion temperature was assumed to be the same as the electron temperature ($T_i = T_e$) during the entire discharge duration. Note that for this case the ion temperature measurements were very inaccurate due to the low central NBI and were not available during the full discharge duration, making these simulations even more relevant for verifying the $T_i = T_e$ hypothesis.

The good match between the measured and calculated neutron rates (figure 14(b)) shows that the $T_i = T_e$ approximation is indeed quite justified in this pulse, particularly after $t = 35$ s, where the T_i measurements were unavailable. Note that the neutron rate values are much lower than the ones for the high power 30 s pulse (figure 12(b)) so the discrepancies between the measured and calculated neutron rates seen in parts of the pulse are actually quite small. Because of the limited NBI power, pulse #105750 features larger electron heating than ion heating in general (see figure 14(c)). During the combined NBI + ICRF phase ($t < 43$ s), the electron and ion heating sources are almost equilibrated (the electrons being slightly dominant due to the ohmic power contribution), while during the NBI only phase the ion heating is decreased because of the lower critical energy characteristic of the colder plasma conditions (see figure 7(f)). The power deposition profiles (figure 15) show indeed very similar

electron and ion absorption during the first phase of the pulse (a). During the NBI-only phase (b), the power absorption is much broader since most of the NB injectors have off-axis deposition, but ion heating is still marginally dominant in the plasma core. Compared to the 30 s discharges with higher NBI power and lower plasma collisionality, the non-inductive current drive contribution from NBI and bootstrap current is smaller (figure 14(b)) but steady in this pulse, representing ca. 17% of the total plasma current. The current diffusion time based on the neo-classical resistivity at $\rho_{\rm norm} = 0.5$ is about $\tau_d = 15$–20 s, suggesting that pulse #105750 was long enough for the current profile to reach steady much before the end of the discharge.

5. Extension to the CICLOP database

The long pulses performed in JET-ILW were added to the international inter-machine database from the 'CICLOP' group, chaired by *Litaudon et al* [55]. Even if JET is not designed for reactor-relevant long discharges—which is the main analysis topic of this working group—the contribution of the experiments described here is significant because currently very few long pulse data is available in the MA-range of plasma current with $T_{\rm i} \approx T_{\rm e}$ and H-mode condition with relevant energy confinement times.

Figure 16 shows the total input energy applied to various discharges in different magnetic confinement fusion devices around the world as function of the high-performance discharge duration. Each data point corresponds to a single discharge performed in a given device. The new JET-ILW long pulses (labeled JETILW-LP to compare with the past JETC Carbon data and the JETILW original data) are depicted as gold diamonds and the black contours indicate machines with metallic plasma facing components. One sees that the new JETILW-LP pulses fall in the intermediate duration and energy range of the database, but they have significantly higher input energy than the previous JET pulses (both with the W/Be-wall JETILW as during the C-wall JETC operations before 2011), reaching the record energy input ever achieved in JET of $E_{\rm IN} = 450$ MJ in the 30 s long pulse #105468 described in section 2.

At this point it is important to place JET's main engineering parameters in the context of the multi-machine CICLOP database. In figure 17 the plasma volume (a) and the averaged plasma current (b) of the various discharges included in the CICLOP database are shown. The JET plasmas are the largest ones in the database, with an average volume of 70–90 m^3, followed by the JT60U data (with shot #48158 approaching the JET values). The Tore-Supra, LHD, DIII-D, and W7-X devices—all with a Carbon wall—are of intermediate size ($V = 20$–30 m^3) and the former two are out of operation. The remaining operational devices with long pulse capability (EAST, KSTAR and WEST) are producing plasmas with $V = 10$–15 m^3. Similarly, figure 17(b) shows that JET operates at higher plasma currents than the other devices (up to $I_{\rm P} = 4.5$ MA for short pulses) and, for discharges with more than 30 s duration, it is the only tokamak contributing with

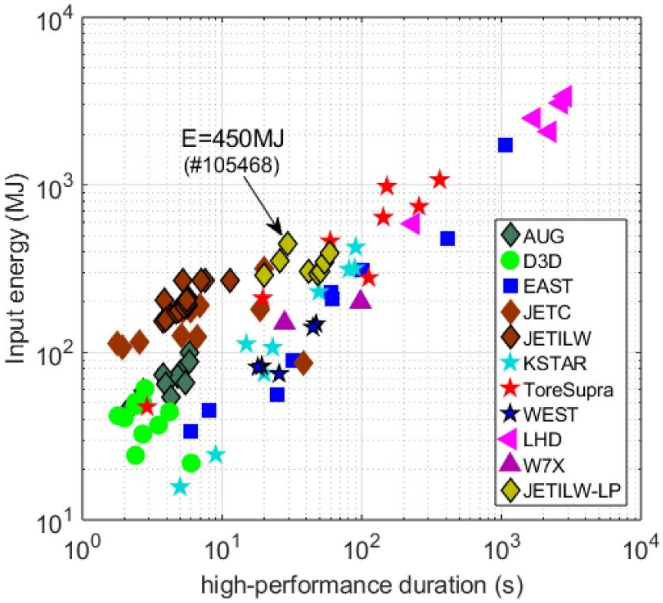

Figure 16. Total input energy as function of the high-performance discharge duration for many devices in the CICLOP database (log scale). The new JETILW-LP data is shown as gold diamonds.

data above 1 MA ($I_{\rm P} = 1.4$ MA in the pulses discussed here). Note that slightly shorter pulses were performed in KSTAR and in JT60U with $I_{\rm P} \approx 1.0$ MA.

Figure 18 shows the time averaged thermal energy confinement time $\tau_{\rm E}$ calculated for the same set of discharges as shown in figure 14. The new JETILW-LP data are clearly above the other points in the database in the $t = 30$–60 s plasma duration range, reaching $\tau_E = 0.2$ s in the high power ($\approx$15 MW) 30 s pulses and up to $\tau_E = 0.3$ s in the low power (6 MW) 60 s pulses. This is aligned with the confinement power degradation expected from the IPB98(y,2) scaling law [72], confirmed in JET at intermediate input power levels [71]. In high-performance/high-beta scenarios developed in JET-ILW with carefully tuned control parameters, this effect was observed to be less strong than what is predicted by the IPB98(y,2) scaling law [6, 25, 80–82]. Note that one pulse from JT60U (#48158) [83] reaches comparable τ_E values to the new JETILW-LP data in the $t = 20$–30 s plasma duration range.

One of the most important contributions of the JET-ILW long pulse experiments to the CICLOP database is in terms of the core plasma ion temperature. As shown in figure 19, the central ion temperature data for the new JETILW-LP pulses—measured by a combination of CXRS and XCS—exceed most of the values obtained in other machines capable of $t > 30$ s pulses. An exception is the 60 s long pulse #34181 performed in Tore-Supra [84], which has the same average $T_{\rm i0}$ value as the 60 s long pulse #105750 done in JET-ILW, $T_{\rm i0} \approx 3$ keV. As a matter of fact, comparable ion temperatures were obtained in Tore-Supra and LHD for longer discharges since these devices were less constrained in terms of the auxiliary input power duration than JET. The central ion temperatures obtained in the JETILW-LP pulses are higher in the 20–30 s dataset, where

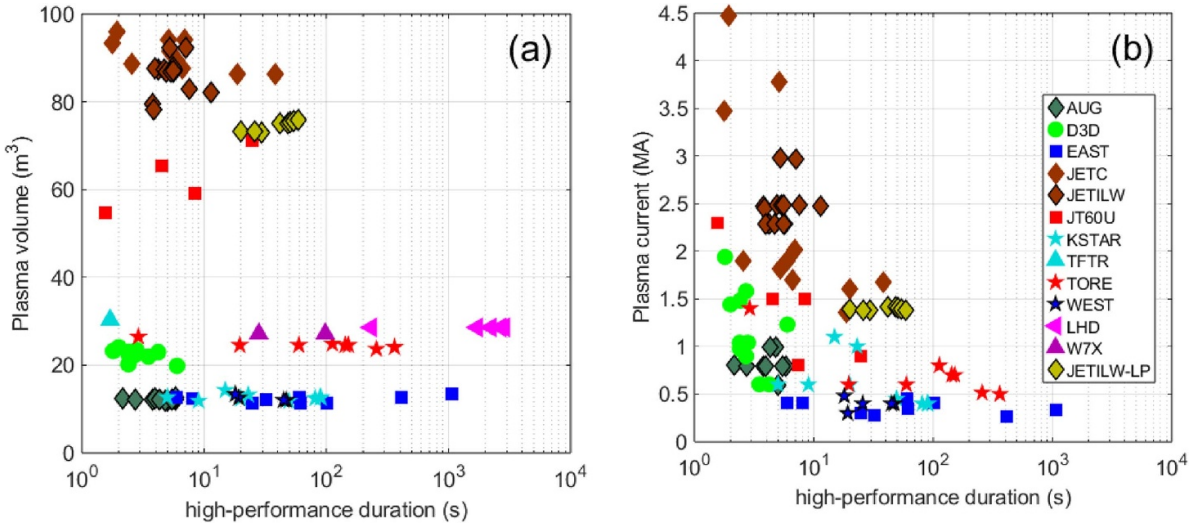

Figure 17. (a) Plasma volume and (b) average plasma current as function of the high-performance discharge duration for the data in the CICLOP database.

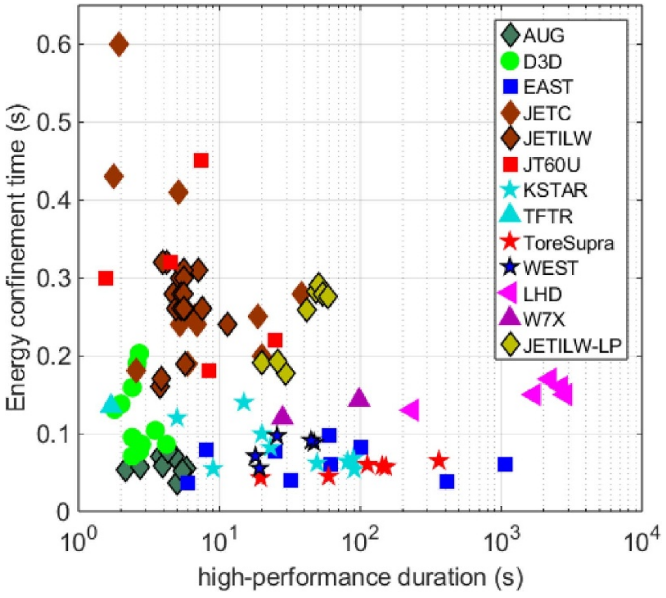

Figure 18. Time averaged energy confinement time as function of the high-performance discharge duration for many devices in the CICLOP database. The new JETILW-LP data is shown as gold diamonds. The highest confinement time is achieved in the medium-power 50–60 s target pulses.

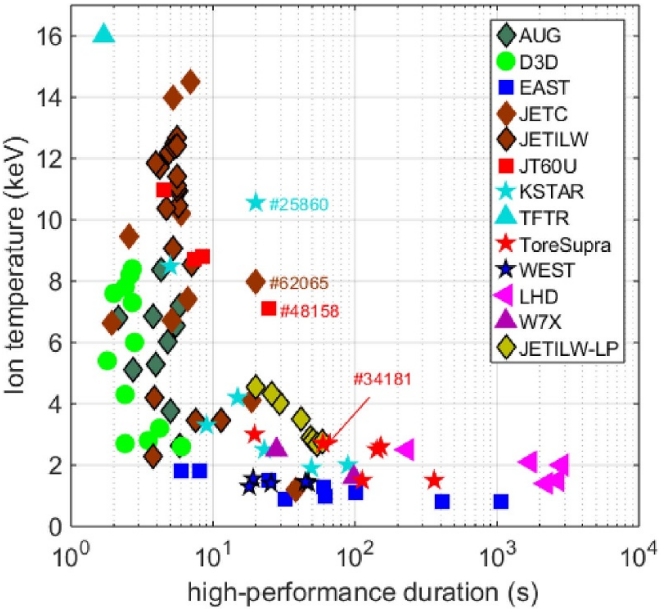

Figure 19. Averaged central ion temperature (CXRS/XCS) as function of the high-performance discharge duration for the different devices in the CICLOP database. The outstanding high temperature pulses from KSTAR, JT60U and JETC are low density discharges that reach a hot-ion regime.

the NBI power—that provides the main ion heating source in JET—is larger ($P_{\mathrm{NBI}} = 12$–14 MW) and decrease linearly with plasma duration because of the limitations on the auxiliary heating power supplies capability. It is interesting to note the remarkable core ion temperatures reached in KSTAR (#25860) [85], JET-C (#62065) [86] and JT60U (#48158) [83] in the $t = 20$–25 s pulse duration range. These pulses are characterized by very low plasma densities ($n_{\mathrm{e0}} < 2$–$3\mathrm{x}10^{19}$ m^{-3}) and high input power, leading to a regime similar to the so called hot-ion mode observed in several devices [87–89]. The central ion pressure values of these discharges (not shown) are actually comparable to the other data points in the $t = 20$–30 s duration domain.

As shown earlier in the paper, the ion (and electron) temperatures in the JET-ILW long pulses varied significantly during the discharges depending on the available NBI power, ICRH power, strike point position, etc. In addition, the core charge exchange measurements depend on specific NB injectors (with central power deposition) [60, 61], which were not available during the full duration of the discharges. Therefore, on top of the large inaccuracies inherent of the CXRS measurements in the plasma core with moderate NBI power, the standard

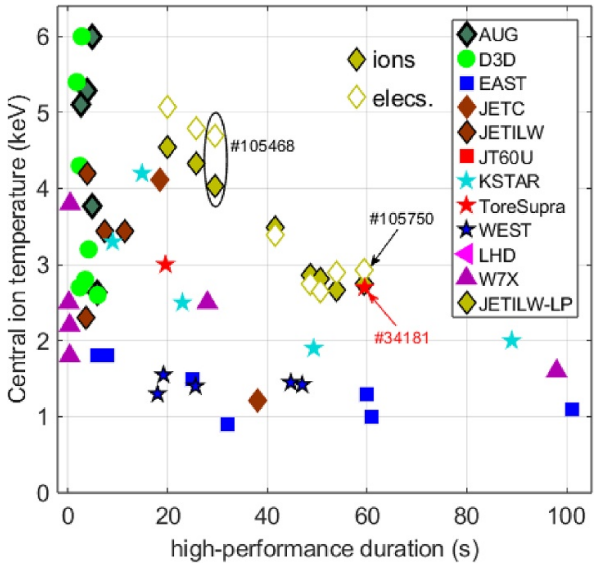

Figure 20. Zoom on the time averaged central ion temperature ($\rho = 0.2$, full symbols, CXRS/XCS) and central electron temperature ($\rho = 0$, open symbols, HRTS, ECE) obtained in JET-ILW as function of the high-performance discharge duration. The error bars of the averaged T_i values in these pulses are rather large (approx. ± 1 keV). Some data points shown in figure 19 are outside of the plot limits of figure 20.

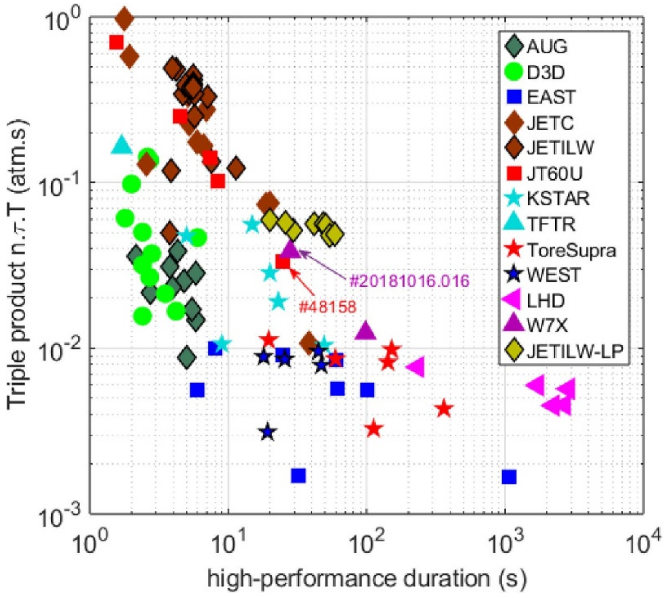

Figure 21. Averaged triple fusion product $n_i.\tau_E.T_i$ as function of the high-performance discharge duration for the different fusion devices in the CICLOP database. The long pulse JETILW-LP data shows low performance degradation because of the larger energy confinement time obtained in the $t = 40$–60 s discharges.

deviation of the time averaged T_i values shown in figure 19 for the JETILW-LP data points is rather large (approx. ± 1 keV).

Figure 20 zooms on the temperature data obtained in the JETILW-LP dataset, where the averaged central electron temperature values (measured by HRTS or ECE) are shown as open symbols for comparison with the T_i values (full symbols), illustrating that in these discharges core electron and ion temperatures were comparable and clearly above the other points in the database (except for the 60 s Tore-Supra pulse #34181 mentioned before [84]). The decrease in the T_e and T_i values observed in the JETILW-LP pulses is due to the auxiliary power limitation and not due to the discharge performance degradation, as seen in figure 18. TRANSP simulations done by assuming $T_i \approx T_e$ have shown good agreement between the calculated and the total measured neutron rate in all phases of these pulses, further supporting the $T_i \approx T_e$ hypothesis (see figures 12 and 14). It is interesting to note that, despite the large inaccuracies on the temperature data, the electron temperature values have the tendency to be larger in the 30 s high power pulses while they practically match the ion temperature measurements in the 60 s medium power pulses. This is explained by the fact that, despite the larger P_{NBI} power applied to the 30 s pulses, ICRH—which produces localized central electron heating in these cases—was available during the full duration of the pulse while for the 60 s it could only be applied on part of the discharge ($\Delta t = 36$ s), leading to more equilibrated time averaged electron and ion temperature data in the latter. The lower electron temperatures achieved in the 60 s pulses leads to higher plasma collisionality, which also contributes to a more efficient electron-ion energy equipartition.

To conclude, figure 21 shows how the new JET-ILW long pulse data contribute to the Kikuchi diagram in the current version of the CICLOP database. The triple product $n_i.\tau_E.T_i$ is calculated using the time averaged values of the respective quantities during the high power duration of the discharges. The ion dilution was very small in these pulses (<3%) so $n_i = n_e$ was considered for simplicity. For the pulses in which the ion temperature measurements were not available throughout the discharge, $T_i = T_e$ was assumed to extend the data to the full discharge duration. This is supported by TRANSP simulations (section 4).

Aside from a $t = 30$ s W7-X pulse (#20181016.016) with high density [90–92] and the $t = 25$ s long JT60U pulse (#48158) with very high ion temperature [83], the new JET-ILW data points clearly stand out in terms of long pulse fusion performance and show almost no degradation in terms of the high-performance discharge duration, with an average value of $n_i.\tau_E.T_i = 0.05$–0.06 atm.s (0.3–0.4×10^{20} m^{-3} keV s) for all points. This is because the lower power $t = 40$–60 s JET pulses feature a larger energy confinement time than the $t = 20$–30 s pulses (see figure 18), which compensates for the lower core ion temperatures achieved with less input power (figure 19). Note that for pulse durations $t > 30$ s, the new JET-ILW data represent a remarkable contribution to the CICLOP database, featuring almost five times larger $n.\tau.T$ values than the other points currently in the database with comparable duration, suggesting that the plasma performance degradation previously documented with the available data shown in figure 21 is pessimistic [55]. Very recent results from W7-X (not yet published) corroborate this statement and achieved comparable $n.\tau.T$ values up to $t = 43$ s. It is worth reiterating that the JET-ILW pulses did not suffer from any physics limitations and

were mainly restricted in duration by machine specific engineering constrains, in particular the auxiliary heating power capabilities and the divertor heat load limits.

6. Summary and conclusions

In the last months of JET operation in 2023, long duration discharges with $I_P = 1.4$ MA and $B_0 = 1.9$ T ($q_{95} \approx 4, f_{GW} \approx 0.7$) were executed to challenge the machine engineering capabilities in an inertially cooled environment with high input power and to assess potential physics limitations of executing long pulses with combined electron and ion heating and good confinement in a large tokamak with metallic walls.

Two types of long duration discharges were developed for this purpose: 30 s high power pulses with combined 12–14 MW NBI and 2 MW ICRH and 60 s long pulses with 4–6 MW NBI and 2 MW ICRH. Both scenarios were in H-mode with regular type-I ELMs, low global radiation levels and no sign of core impurity accumulation nor deleterious MHD activity. In general, none of the long pulses suffered from any physics limitation and the plasma performance and maximum duration were limited by engineering constrains, namely the auxiliary power availability, the divertor heat exhaust capability and lack of non-inductive current-drive [48]. Because NBI provides efficient core ion heating in JET while ICRH—using H minority heating—provides localized electron heating near the magnetic axis, these pulses featured comparable core electron and ion temperatures, reaching 5 keV in the high power 30 s pulses and about 3 keV in the medium power 60 s pulses during the combined ICRH and NBI heating phase, with energy confinement times between $\tau_E = 0.2$–0.3 s.

In the high power 30 s pulses, the ELM dynamics showed strong dependence on the strike point position at given power and gas injection rate while in the 60 s pulses, the input power was close to the L–H threshold and the type-I ELMs were smaller with a frequency very sensitive to the value of the power through the separatrix.

The 30 s pulses achieved the maximum input energy ever in JET history, $E_{IN} = 450$ MJ, and the inertially cooled divertor reached thermal equilibrium after approximately 20 s without visible signs of overheating. The 60 s pulses were the longest ever done in JET in the last 30 years but, because of the lower averaged input power compared to the 30 s pulses, they featured lower divertor temperatures and never fully reached thermal equilibrium. A few of the 30 s and 60 s discharges exceeded the normal energy limits imposed for the horizontal bulk W divertor plates without any signs of post-pulse damage. The Be main chamber temperatures were very low (<400 °C) in all the discharges performed without any sign of hot-spot formation. These experiments also provided an excellent test-bed for the novel water activation diagnostic techniques being developed in support of ITER and future fusion reactors, as described in [52, 53].

The results presented here also marked a significant contribution to the international inter-machine CICLOP database [55], currently reaching the highest averaged ion temperatures and triple-fusion product values in the 30–60 s high-performance discharge duration range without deleterious limitations in terms of plasma physics, $n_i.\tau_E.T_i = 0.05$–0.06 atm.s (0.3–0.4×10^{20} m^{-3} keV s), and suggested that the data currently available in the CICLOP database is providing a pessimistic extrapolation to $t > 30$ s duration discharges in terms of fusion performance. Recent results from W7-X (not yet published) corroborate this statement and indicate that the decrease in fusion performance (or triple-product) observed with pulse duration in the current multi-machine databases is generally related to engineering rather than physics constrains (e.g. heating power capabilities or first-wall localized heating) but that physics limitations such as poor confinement, impurity accumulation or ion temperature clamping [93] may also play a role. This discussion will be left for a future publication.

Long pulse development is one of the main activities pursued in current tokamaks and stellarators. At every experimental campaign world-wide, physics and engineering limits are challenged and exciting updates to the CICLOP database are readily taking place. During the compilation of this publication, new world-records were meanwhile achieved in terms of long plasma operation, with pulse durations exceeding $t = 1000$ s in the EAST and WEST tokamaks. These extraordinary results—only met in LHD in the past—are being published elsewhere [94–97] and will be added to the CICLOP database in due time.

For designing and operating future fusion reactors, it is important to disentangle between machine specific engineering constrains (auxiliary heating capability, wall/divertor cooling capability, current-drive efficiency, etc.) and plasma physics limitations (resistive wall modes, MHD, plasma-wall interactions, impurity accumulation, ion temperature clamping, etc.). This type of discharge duration limit classification will be given special attention in future CICLOP activities.

Data availability statement

All data that support the findings of this study are included within the article (and any supplementary files).

Acknowledgments

This work has been carried out within the framework of the EUROfusion Consortium, funded by the European Union via the Euratom Research and Training Programme (Grant Agreement No 101052200—EUROfusion). Views and opinions expressed are however those of the author(s) only and do not necessarily reflect those of the European Union or the European Commission. Neither the European Union nor the European Commission can be held responsible for them. The views and opinions expressed herein do not necessarily reflect those of the ITER Organization.

ORCID iDs

E Lerche 0000-0003-4584-3581
X Litaudon 0000-0001-6973-9717
S Brezinsek 0000-0002-7213-3326

E Joffrin 0009-0008-7527-0984
A Boboc 0000-0001-8841-3309
I S Carvalho 0000-0002-2458-8377
E Delabie 0000-0001-9834-874X
R Felton 0009-0002-2287-676X
N Fonnesu 0000-0002-2800-0040
S Gerasimov 0009-0002-3793-7211
S Hotchin 0009-0009-8414-2658
K Kirov 0000-0001-8104-4782
M Maslov 0000-0001-8392-4644
D Matveev 0000-0001-6129-8427
I Monakhov 0009-0009-2936-5605
M Poradzinski 0000-0002-1858-4046
F Rimini 0009-0001-2917-0455
S Silburn 0000-0002-3111-5113
E R Solano 0000-0002-4815-3407
H Sun 0000-0003-0880-0013
D Van Eester 0000-0002-4284-3992

References

[1] Matthews G F *et al* 2011 *Phys. Scr.* **2011** 014001
[2] Neu R *et al* 2011 *Plasma Phys. Control. Fusion* **53** 124040
[3] Horton L *et al* 2013 *Fusion Eng. Des.* **88** 434–9
[4] Joffrin E *et al* 2014 *Nucl. Fusion* **54** 013011
[5] Romanelli F *et al* 2015 *Nucl. Fusion* **55** 104001
[6] Challis C D *et al* 2015 *Nucl. Fusion* **55** 053031
[7] Giroud C *et al* 2015 *Plasma Phys. Control. Fusion* **57** 035004
[8] Litaudon X *et al* 2017 *Nucl. Fusion* **57** 102001
[9] Dumont R J *et al* 2018 *Nucl. Fusion* **58** 082005
[10] Garzotti L *et al* 2019 *Nucl. Fusion* **59** 076037
[11] Solano E R *et al* 2022 *Nucl. Fusion* **62** 076026
[12] Mailloux J *et al* 2022 *Nucl. Fusion* **62** 042026
[13] Arnoux G *et al* 2014 *Phys. Scr.* **2014** 014009
[14] Silburn S A *et al* 2017 *Phys. Scr.* **2017** 014040
[15] Huber A *et al* 2018 *Nucl. Fusion* **58** 106021
[16] Brezinsek S *et al* 2013 *Nucl. Fusion* **53** 083023
[17] Brezinsek S *et al* 2016 *Phys. Scr.* **2016** 014076
[18] Mayer M *et al* 2016 *Phys. Scr.* **2016** 014051
[19] Widdowson A *et al* 2017 *Nucl. Fusion* **57** 086045
[20] Krat S *et al* 2020 *Phys. Scr.* **2020** 014059
[21] Maggi C F *et al* 2024 *Nucl. Fusion* **64** 112012
[22] Joffrin E *et al* 2024 *Nucl. Fusion* **64** 112019
[23] Kappatou A *et al* 2025 *Plasma Phys. Control. Fusion* **67** 045039
[24] Challis C D *et al* 2022 *48th EPS Conf. on Plasma Physics* (*Maastricht (Netherlands)*)
[25] Hobirk J *et al* 2023 *Nucl. Fusion* **63** 112001
[26] Fitzgerald M *et al* 2023 *Nucl. Fusion* **63** 112006
[27] Solano E R *et al* 2023 *Nucl. Fusion* **63** 112011
[28] Garzotti L *et al* 2023 Development of high current baseline scenario for high deuterium-tritium fusion performance at JET *IAEA Fusion Energy Conf.* (*London, 16–21 October 2023*) EX/7–3
[29] Garcia J *et al* 2022 *Phys. Plasmas* **29** 032505
[30] Giroud C *et al* 2024 *Nucl. Fusion* **64** 106062
[31] Maslov M *et al* 2023 *Nucl. Fusion* **63** 112002
[32] Lerche E *et al* 2023 *AIP Conf. Proc.* **2984** 030005
[33] Sharapov S E *et al* 2023 *Nucl. Fusion* **63** 112007
[34] Mantica P *et al* 2024 *Nucl. Fusion* **64** 086001
[35] Kiptily V G *et al* 2024 *Nucl. Fusion* **64** 086059
[36] Bonofiglo P J *et al* 2024 *Nucl. Fusion* **64** 096038
[37] The JET Team (presented by D. Stork) 1993 Plasma physics and controlled nuclear fusion research *1992 Proc. 14th Int. Conf. (Wurzburg)* vol 1 (IAEA) p 445
[38] Ciric D *et al* 2011 *Fusion Eng. Des.* **86** 509–12
[39] King D *et al* 2023 *Nucl. Fusion* **63** 112005
[40] Mayoral M-L *et al* 2014 *Nucl. Fusion* **54** 033002
[41] Monakhov I, Jacquet P, Dumortier P, Durodié F, Lerche E, Lobel R, Mayoral M-L, Noble C, Roberts J and Sheikh H 2025 *Plasma Phys. Control. Fusion* **67** 015023
[42] Murari A *et al* 2016 *IEEE Trans. Nucl. Sci.* **63** 1674–81
[43] Figueiredo J *et al* 2018 *Rev. Sci. Instrum.* **89** 10K119
[44] Villari R *et al* 2016 *Fusion Eng. Des.* **109–111** 895–905
[45] Lehnen M *et al* 2013 *Nucl. Fusion* **53** 093007
[46] Gerasimov S N *et al* 2020 *Nucl. Fusion* **60** 066028
[47] Sheikh U A *et al* 2021 *Nucl. Fusion* **61** 126043
[48] King D *et al*, 'Technical and Engineering challenges for long pulses on JET ITER Like Wall', this PPCF issue
[49] Maggi C F *et al* 2019 *Nucl. Fusion* **59** 076028
[50] Schneider P A *et al* 2023 *Nucl. Fusion* **63** 112010
[51] Waterhouse J, Wheatley M, Stephen A, Hogben C, Jones G, Goodyear A, Farmer T and McCullen P 2025 *Fusion Eng. Des.* **210** 114737
[52] Radulović V, Rupnik S, Naish J, Bradnam S, Ghani Z, Popovichev S, Kiptily V, Batistoni P, Villari R and Snoj L 2021 *Fusion Eng. Des.* **169** 112410
[53] Villari R *et al* 2025 *Fusion Eng. Des.* **217** 115133
[54] Matveev D *et al* 2024 private communications
[55] Litaudon X *et al* 2024 *Nucl. Fusion* **64** 015001
[56] Huber A *et al* 2007 *Fusion Eng. Des.* **82** 1327–34
[57] Ferreira D, Carvalho P J, Carvalho I S, Stuart C and Lomas P J 2021 *Fusion Eng. Des.* **164** 112179
[58] Pasqualotto R, Nielsen P, Gowers C, Beurskens M, Kempenaars M, Carlstrom T and Johnson D 2004 *Rev. Sci. Instrum.* **75** 3891–3
[59] Maggi C F *et al* 2012 *Rev. Sci. Instrum.* **83** 10D517
[60] Negus C R, Giroud C, Meigs A G, Zastrow K-D and Hillis D L 2006 *Rev. Sci. Instrum.* **77** 10F102
[61] Hawkes N, Delabie E, Menmuir S, Giroud C, Meigs A G, Conway N J, Biewer T M and Hillis D L 2018 *Rev. Sci. Instrum.* **89** 10D113
[62] Shumack A E *et al* 2014 *Rev. Sci. Instrum.* **85** 11E425
[63] Joffrin E *et al* 2017 *Nucl. Fusion* **57** 086025
[64] Maggi C F *et al* 2015 *Nucl. Fusion* **55** 113031
[65] Field A *et al* 2022 *Nucl. Fusion* **63** 016028
[66] King D B *et al* 2025 JET hybrid scenario development in D-T for impurity screening study *30th IAEA Fusion Energy Conf.*
[67] Snyder P B, Wilson H R, Ferron J R, Lao L L, Leonard A W, Osborne T H, Turnbull A D, Mossessian D, Murakami M and Xu X Q 2002 *Phys. Plasmas* **9** 2037
[68] Nyström H, Frassinetti L, Saarelma S, Huijsmans G T A, Perez von Thun C, Maggi C F, Hillesheim J C and contributors J 2022 *Nucl. Fusion* **62** 126045
[69] Saarelma S, Frassinetti L, Bilkova P, Challis C D, Chankin A, Fridström R, Garzotti L, Horvath L and Maggi C F 2019 *Phys. Plasmas* **26** 072501
[70] de la Luna E, Sánchez J, Tribaldos V, contributors J-E, Conway G, Suttrop W, Fessey J, Prentice R, Gowers C and Chareau J M 2004 *Rev. Sci. Instrum.* **75** 3831–3
[71] Nunes I *et al* 2016 *Plasma Phys. Control. Fusion* **58** 014034
[72] ITER Physics Basis 1999 *Nucl. Fusion* **39** 2232
[73] Martin Y R and Takizuka T (the ITPA CDBM H-mode Threshold Database Working Group) 2008 *J. Phys.: Conf. Ser.* **123** 012033
[74] Solano E R *et al* 2017 *Nucl. Fusion* **57** 022021
[75] Goldston R J, McCune D C, Towner H H, Davis S L, Hawryluk R J and Schmidt G L 1981 *J. Comput. Phys.* **43** 61–78
[76] Lao L L, St John H, Stambaugh R D, Kellman A G and Pfeiffer W 1985 *Nucl. Fusion* **25** 1611
[77] Meneghini O *et al* 2015 *Nucl. Fusion* **55** 083008
[78] Štancar Ž *et al* 2023 *Nucl. Fusion* **63** 126058
[79] Hirshman S P 1988 *Phys. Fluids* **31** 3150

[80] Joffrin E *et al* 2010 *23rd IAEA Fusion Energy Conf.* (*Daejon, Republic of Korea*)
[81] Mantica P *et al* 2011 *Phys. Rev. Lett.* **107** 135004
[82] Hobirk J *et al* 2022 *48th EPS Conf. on Plasma Physics* (*Maastricht (Netherlands)*)
[83] Oyama N *et al* 2009 *Nucl. Fusion* **49** 104007
[84] Jacquinot J *et al* 2005 *Nucl. Fusion* **45** S118
[85] Han H *et al* 2022 *Nature* **609** 269–75
[86] Joffrin E *et al* 2005 *Nucl. Fusion* **45** 626–34
[87] Clarke J F 1980 *Nucl. Fusion* **20** 563
[88] Keilhacker M *et al* 1991 *Plasma Phys. Control. Fusion* **39** B1
[89] Gormezano C *et al* 1999 *Plasma Phys. Control. Fusion* **41** B367
[90] Jakubowski M *et al* 2021 *Nucl. Fusion* **61** 106003
[91] Langenberg A *et al* 2024 *Phys. Plasmas* **31** 052502
[92] Ford O P *et al* 2024 *Nucl. Fusion* **64** 086067
[93] Beurskens M N A *et al* 2021 *Nucl. Fusion* **61** 116072
[94] Song Y *et al* 2023 *Sci. Adv.* **9** eabq5273
[95] Huang J *et al* 2023 *Phys. Plasmas* **30** 062504
[96] Gong X *et al* 2025 Overview of recent experimental results on EAST in support of ITER new research plan *30th IAEA Fusion Energy Conf.* (*Chengdu*)
[97] Dumont R *et al* 2025 Preparing for the operation of next-step fusion devices: long-pulse plasma scenario developments in the WEST tokamak *30th IAEA Fusion Energy Conf.* (*Chengdu*)